# Zwitterion-functionalized SnO₂ Substrate Induced Sequential Deposition of Black Phase FAPbI₃ with Rearranged PbI₂ Residue

*Zhixiao Qin[a], Yuetian Chen[a], Xingtao Wang[a], Ning Wei[a], Xiaomin Liu[a], Haoran Chen[a], Yanfeng Miao[a], and Yixin Zhao[a,b]\**

Dr. Z. Qin, Dr. Y. Chen, X. Wang, N. Wei, X. Liu, H. Chen, Dr. Y. Miao, Prof. Y. Zhao

[a] School of Environmental Science and Engineering, Frontiers Science Center for Transformative Molecules, Shanghai Jiao Tong University, Shanghai 200240, China.

Prof. Y. Zhao

[b] Shanghai Institute of Pollution Control and Ecological Security, Shanghai 200240, China.

E-mail: yixin.zhao@sjtu.edu.cn

Abstract

Black phase formamidinium lead iodide (FAPbI₃) with narrow band gap and high thermal stability has emerged as the most promising candidate for highly efficient and stable perovskite photovoltaics. In order to overcome the intrinsic difficulty of black phase crystallization and to eliminate the PbI₂ residue, most sequential deposition methods of FAPbI₃-based perovskite would introduce external ions like methylammonium (MA⁺), cesium (Cs⁺), and bromide (Br⁻) ions to the perovskite structure of the light absorbing layer. Here we introduce a zwitterion-functionalized SnO₂ as the electron transport layer (ETL) to induce the crystallization of high quality black phase FAPbI₃ on such SnO₂ substrate. The SnO₂ ETL treated with the zwitterion, formamidine sulfinic acid (FSA), can help rearrange the stack direction, orientation and distribution of residual PbI₂ in perovskite layer, which reduces the side effect of the residual PbI₂ to the perovskite structure. Besides, the FSA functionalization also modifies SnO₂ ETL to

suppress the deep-level defects at the perovskite/SnO$_2$ interface. As a result, the FSA-FAPbI$_3$ based perovskite solar cells (PSCs) exhibit an excellent power conversion efficiency up to 24.1% with 1000 h long-term operational stability, which is among the highest values for FAPbI$_3$ PSCs fabricated from sequential deposition. Our findings provide a new interface engineering strategy on the sequential fabrication of black phase FAPbI$_3$ PSCs with improved optoelectronic performance.

## 1. Introduction

Metal halide perovskite solar cells (PSCs) have been extensively investigated in the past decade as the most promising candidate for next generation photovoltaics.[1-3] Among the lead halide perovskite materials, black phase FAPbI$_3$ with relatively narrow bandgap is an ideal candidate to approach the Shockley-Queisser limit.[4] Up to now, most of highly efficient and stable black phase FAPbI$_3$ perovskites are fabricated through one-step deposition using antisolvent, which is not convenient for large-scale fabrication because of its narrow processing windows.[5-7] Another commonly used method of two-step sequential deposition has wide processing windows, which offers several advantages for the production of larger modules. But it is somehow difficult to fabricate FAPbI$_3$ perovskite using this method, which can be ascribed to the difficulty of intercalating FA$^+$ with large ionic radius into the [PbI$_6$]$^{4-}$ framework in sequential deposition. This process could also introduce defects in black phase FAPbI$_3$ perovskite film, which would lead to undesirable non-radiative recombination.[8] To overcome these drawbacks, methylammonium (MA$^+$), cesium (Cs$^+$), and bromide (Br$^-$) ions have been doped into FA-based perovskites via sequential deposition, which can reduce the formation energy of black phase FAPbI$_3$ and inhibit the defects.[9-11] But these doping strategies introduce some side effects such as enlarged bandgap and potential phase segregation issues.[12-14]

The double-edged sword effect of PbI$_2$ residue is another issue in sequential deposition. Moderate residual PbI$_2$ at the grain boundary of perovskite can passivate defects and reduce hysteresis,[15] whereas sometimes the residual PbI$_2$ can deteriorate the photo-stability of PSCs.[16-17] Thus, good control on the concentration and distribution of residual PbI$_2$ also plays a crucial role in

the formation of high-quality black phase $FAPbI_3$ perovskite on the photovoltaic performance. Herein, we report employing a zwitterion of formamidine sulfinic acid (FSA) to functionalize $SnO_2$ layer for sequential deposition of black phase $FAPbI_3$ for highly efficient and stable perovskite photovoltaics. Besides helping with the crystallization of black phase $FAPbI_3$ perovskite, the incorporation of FSA zwitterion can rearrange the stack direction, orientation and distribution of residual $PbI_2$ to reduce its side effect. The FSA zwitterion also acts as interfacial dipole to enhance the conductivity and decrease the work function of $SnO_2$ electron transport layer (ETL). All these advantages help to suppress the deep-level defects for non-radiative carrier recombination and accelerate the electron extraction at the $SnO_2$/perovskite interface. Consequently, $FAPbI_3$ PSCs with the FSA interface engineering strategy achieve an excellent power conversion efficiency (PCE) up to 24.1% and 1000 h long-term operational stability.

## 2. Results and Discussion

Calculations based on density functional theory (DFT) was carried out to map out the electrostatic potential (ESP), which visualizes the charge distribution of the FSA molecule. The chemical structure and the ESP map of FSA zwitterion are shown in **Figure S1** and **Figure 1a**, respectively. A gradual change of color from red to blue on the ESP map indicates a gradual decrease on the degree of electron density from the negative center ($-SO_2^-$ group) toward the positive center ($-C(NH_2)_2^+$ group) in such structure. The molecular dipole moment of FSA is calculated to be 11.86 D, which is higher than many of the previously reported zwitterion molecules that were used for the modification of perovskite photovoltaics (**Table S1**).[18] The zwitterion material FSA was then employed to modify the surface of $SnO_2$ ETL by a two-stage spin-coating process (**Figure S2**). X-ray photoelectron spectroscopy (XPS) measurement was then carried out to analyze the bonding state of $SnO_2$ with FSA modification (noted as FSA-$SnO_2$). As shown in XPS spectra (**Figure S3**), the peaks of N 1s and S 2p appear after FSA was added, and the peak intensities increase with FSA concentration. Importantly, the peaks of Sn 3d and O 1s shift to higher binding energies as compared to those for control $SnO_2$. This can be attributed to

3

the chemical interaction of Sn with the electronegative O in FSA molecule.[19] The effects of FSA on the surface energy levels of SnO$_2$ ETL were studied *via* ultraviolet photoelectron spectroscopy (UPS). As shown in **Figure 1b**, the work function (WF) and valence band maximum (VBM) were calculated from the binding energy cutoff of secondary electron in the range of 15-19 eV and the onset in the range of 1-7 eV, respectively. The WF of SnO$_2$ ETL shift from 4.36 eV to 4.14 eV *via* FSA modification, and this energy level shift confirms the interfacial dipole effects of the proposed zwitterion.[20] The conduction band minimum (CBM) of the SnO$_2$ ETL was derived from the VBM and the bandgap (E$_g$) values determined using ultraviolet visible (UV-vis) absorption spectroscopy (**Figure S4**). The detailed values are listed in **Table S2**. Therefore, as displayed in **Figure 1c**, the interfacial dipole effect from FSA modification can improve the energy level alignment and electronic coupling between SnO$_2$ ETL and perovskite, accelerating the electron extraction and preventing the hole transport.

Atomic force microscopy (AFM) characterization was carried out to study the effect of FSA treatment on the surface roughness of SnO$_2$ ETL. As shown in **Figure 1d**, FSA-SnO$_2$ displays a reduced root-mean-square (RMS) on surface roughness of 1.24 nm compared to that of pristine SnO$_2$ (1.46 nm). The smoother surface can facilitate a close contact between SnO$_2$ ETL and perovskite, which is beneficial to the crystallization of high-quality black phase FAPbI$_3$. The change in the conductivity of SnO$_2$ ETL by FSA treatment is confirmed by the conductive AFM (c-AFM). As shown in **Figure 1e**, the FSA-SnO$_2$ ETL exhibits generally enhanced current in the scan region. We speculate that the enhanced conductivity is ascribed to charge redistribution on the surface of FSA-SnO$_2$ ETL by the strong interaction between SnO$_2$ and FSA molecule. To confirm our speculation and gain insight into the experimental results, theoretical calculations were performed using DFT. As mentioned above, the O of FSA molecule can bond with the Sn on the surface of SnO$_2$, as illustrated in **Figure S5**. Charge density difference of FSA on SnO$_2$ (110) surface is calculated to explore the interaction between SnO$_2$ and FSA molecule (**Figure 1f**). The blue regions represent electron depletion from relative bonds or atoms after charge redistribution, while the yellow regions denote electron accumulation. The resulting electron

clouds at the interface demonstrate that Sn atoms obtain the electrons from FSA molecule through Sn-O bond. Strikingly, more accepted electron clouds spread to peripheral Sn atoms other than the directly connected Sn atoms in the redistribution, which indicates the electrons accepted by the peripheral Sn atoms at the surface are delocalized (**Figure S6**). The amount of delocalized electrons on Sn atoms of FSA-SnO$_2$ surface has been remarkably augmented, leading to the improved conductivity of SnO$_2$ ETL. Kelvin probe force microscopy (KPFM) results further confirm the increased surface potential of FSA-SnO$_2$ ETL, suggesting that the delocalized electrons can also cause the change of electrical field on surface (**Figure S7**).
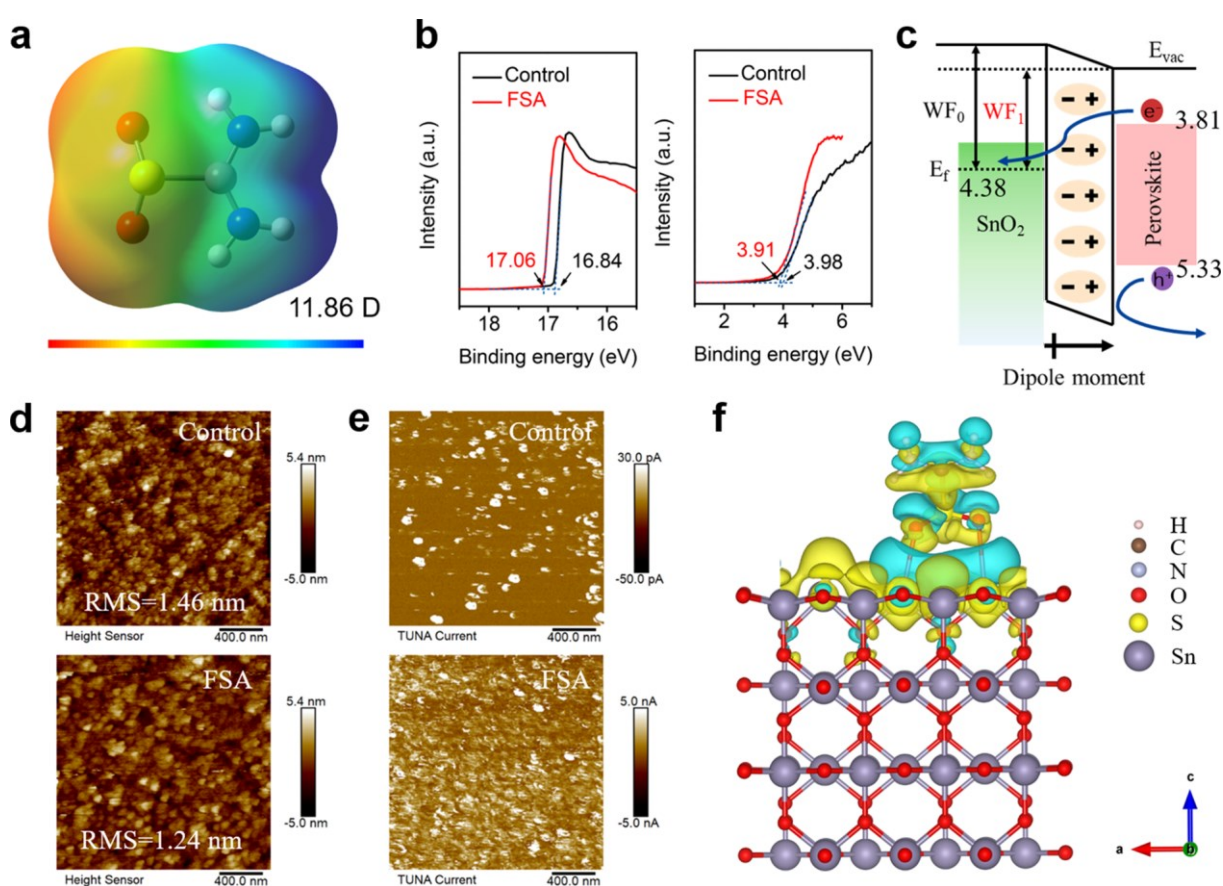


**Figure 1.** (a) ESP map of FSA zwitterion. (b) UPS spectra of SnO$_2$ and FSA-SnO$_2$ films. (c) Schematic illustration of the energy diagram. (d) AFM images and (e) c-AFM images of SnO$_2$ and FSA-SnO$_2$ films. (f) Charge density difference of FSA on SnO$_2$ (110) surface at isovalue of 5×10$^{-3}$ electrons/Å$^3$. Yellow indicates electron accumulation and blue indicates electron depletion.

We herein obtained two-dimensional (2D) patterns using grazing-incidence wide-angle X-ray scattering (GIWAXS) to probe changes in the crystallographic orientations of the precursor $PbI_2$ and perovskite crystals after FSA modification (**Figure 2a** and **2c**). The ring at the scattering vector $q \approx 9$ $nm^{-1}$ corresponds to the (001) plane of $PbI_2$ and the ring at $q \approx 10$ $nm^{-1}$ is assigned to the (100) plane of black phase $FAPbI_3$. As displayed in **Figure 2b**, $FSA-PbI_2$ film shows a sharper peak near the azimuthal angle of 90° by normalizing the intensity of (001) diffraction of $PbI_2$, suggesting the $PbI_2$ crystals have more vertically oriented crystallization in $FSA-PbI_2$ film.[21] Thus, the sequentially added $FA^+$ can quickly intercalate into the $[PbI_6]^{4-}$ framework and completely react with $PbI_2$ to form a stable black phase $FAPbI_3$ structure in the second step.[22-23] Besides, the subsequent perovskite films both exhibit (001) diffraction of $PbI_2$ and (100) plane of $FAPbI_3$. As shown in **Figure 2d**, an obvious peak at around 90° represents a highly vertically oriented $FSA-FAPbI_3$ perovskite film, which introduces a better charge transport in the bulk perovskite.

In particular, compared to the control perovskite, a strong spot of $PbI_2$ (001) plane at azimuthal angle of 90° is observed in **Figure 2c**, revealing the high orientation on (001) plane of residual $PbI_2$ in $FSA-FAPbI_3$ tends to stack along the face-up direction (**Figure S8 and S9**). These results suggest that $FSA-SnO_2$ substrate can regulate the stack direction and orientation of residual $PbI_2$ in perovskite, which was further confirmed by top-view scanning electron microscopy (SEM) and AFM images. As displayed in **Figure 2e and Figure S10**, a lot of disordered residual $PbI_2$ is observed on the surface of control perovskite, while residual $PbI_2$ stacks along the vertical direction and distributes regularly at grain boundaries of $FSA-FAPbI_3$. The concentration of residual $PbI_2$ is reduced with the increased amount of FSA modification (**Figure S11**), which is consistent with the X-ray diffraction (XRD) results (**Figure S12**). Meanwhile, the cross-sectional SEM images (**Figure 2f**) clearly confirm that $FSA-SnO_2$ substrate can effectively inhibit residual $PbI_2$ at the bottom of perovskite film. Recent studies have been demonstrated that the excess $PbI_2$ accumulated at the ETL/perovskite interface will block the

electron transport and cause degradation under illumination.[24] Thus, the construction of our FSA-$SnO_2$ substrate can affect the stack direction, orientation and distribution of residual $PbI_2$, suppressing the side effect of the residual $PbI_2$ in $FAPbI_3$ perovskite.
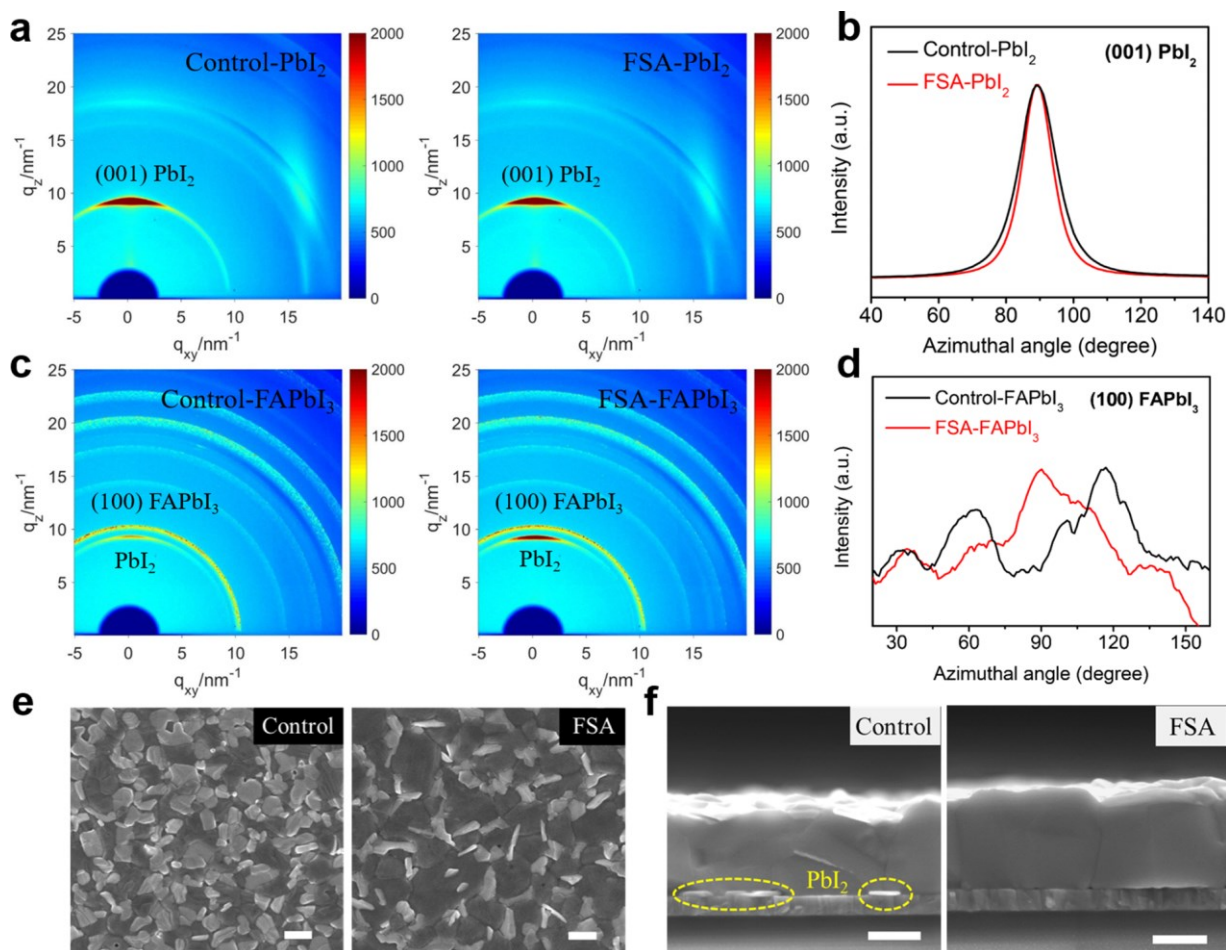


**Figure 2.** (a) 2D GIWAXS patterns of the control and FSA-$PbI_2$ films. (b) The intensity azimuthal graph of (001) diffraction of $PbI_2$ prepared under both conditions. (c) 2D GIWAXS patterns of the control and FSA-$FAPbI_3$ perovskite films. (d) The intensity azimuthal graph of (100) diffraction of $FAPbI_3$ perovskite prepared under both conditions. (e) Top-view SEM images (scale bar: 1μm), and (f) cross-sectional SEM images (scale bar: 500 nm) of control and FSA-$FAPbI_3$ perovskite films.

To locate the distribution of FSA zwitterion in $FAPbI_3$ perovskite film, time-of-flight secondary ion mass spectroscopy (ToF-SIMS) measurements were carried out. As shown in **Figure 3a**, the depth profile of the characteristic S anion in FSA clearly shows the distribution of FSA at the $SnO_2$

ETL/perovskite interface. The 3D depth profile of S anions gives more distinct evidence for this phenomenon (**Figure 3b**). The above results further reveal that FSA acts as interfacial dipole to connect the $SnO_2$ ETL and perovskite layer, rather than diffusing into $FAPbI_3$ perovskite layer. According to the comparison on the XPS data of perovskite films before and after the FSA modification (**Figure S13**), we also confirm that the zwitterion FSA does not affect the surface chemical states of perovskite films. **Figure 3c** shows the UV-vis absorption and the steady-state photoluminescence (PL) spectra of the control and FSA-$FAPbI_3$ films. Identical absorption onsets (**Figure S14**) as well as PL peaks at 814 nm can be found, which implies that the FSA-$SnO_2$ substrate does not induce a bandgap change of perovskite. Besides the steady-state PL, time-resolved PL (TRPL) measurements were also performed to investigate the charge carrier dynamics in $FAPbI_3$ perovskite. Compared with control sample, a significant PL quenching is observed in the FSA-$SnO_2$/perovskite film (**Figure 3c**). Such PL quenching is a representative of a curtailed charge carrier recombination lifetime, which has been monitored by TRPL decay. As depicted in **Figure 3d**, the TRPL lifetime of $SnO_2$/perovskite film decreases from 149 ns to 83 ns with FSA modification. The PL quenching and shortened recombination lifetime indicate efficient electron extraction at the FSA-$SnO_2$ ETL/perovskite interface.[25] Moreover, as shown in **Figure 3e**, the transient photocurrent (TPC) decay of FSA-$FAPbI_3$ based device shows faster photocurrent decay response (7.96 µs) than that of the control device (15.25 µs), which further illustrates faster charge transport on FSA-$SnO_2$ substrate.

The performance of PSCs is closely associated with defect-dependent charge carrier recombination behavior. The transient photovoltage (TPV) decay curves in **Figure 3f** reveal that the FSA-$FAPbI_3$ based device shows a longer lifetime (1.03 ms) than that of control device (0.32 ms), indicating a significant decrease of charge carrier recombination.[26] We also used the electrochemical impedance spectroscopy (EIS) measurement to investigate the electrical properties and charge recombination behavior in FSA-$FAPbI_3$ perovskite devices. As shown in **Figure 3g**, a higher recombination resistance ($R_{rec}$) is observed with FSA treatment (1209 kΩ) than that of control device

8

(386 kΩ), suggesting the reduced carrier recombination loss in PSCs. The formation of dark current is caused by the migration of charge carriers due to the existed defects in PSCs. As shown in **Figure S15**, the FSA-FAPbI$_3$ PSC displays generally lower dark current densities compared to that of the control PSC within the voltage range from -1.0 to 1.0 V, further confirming the passivation effect of FSA-SnO$_2$ substrate. To further quantitatively investigate the function of FSA modification on the defect density of FAPbI$_3$ perovskite, electron-only devices were prepared and measured by space-charge-limited-current (SCLC) method. As displayed in **Figure 3h**, the trap-filled limited voltage (V$_{TFL}$) is the transition voltage between ohmic and trap-filling regions. The defect density value (N$_t$) can be determined by the following equation:[27]

$$N_t = \frac{2\varepsilon\varepsilon_0 V_{TFL}}{eL^2}$$

where $\varepsilon_0$ is the vacuum dielectric constant, $\varepsilon$ is the relative dielectric constant, e is the elemental charge, and L is the thickness of the perovskite film. The defect density of FAPbI$_3$ perovskite is appreciably reduced from $4.39 \times 10^{15}$ to $2.26 \times 10^{15}$ cm$^{-3}$ with FSA modification. This phenomenon is in good agreement with the results of TPV, EIS, and dark current density-voltage (*J-V*) characterizations, which further confirms the reduced defects for unfavored recombination in FSA-FAPbI$_3$ PSCs. The recombination mechanism in PSCs can also be investigated by ideality factor (n$_{id}$), which can be extracted from analyzing the relationship between the *V*$_{OC}$ and light intensity. As displayed in **Figure S16**, the n$_{id}$ value reduces from 1.81 to 1.34 for FSA-FAPbI$_3$ based PSCs, indicating that the undesired charge recombination is effectively suppressed.
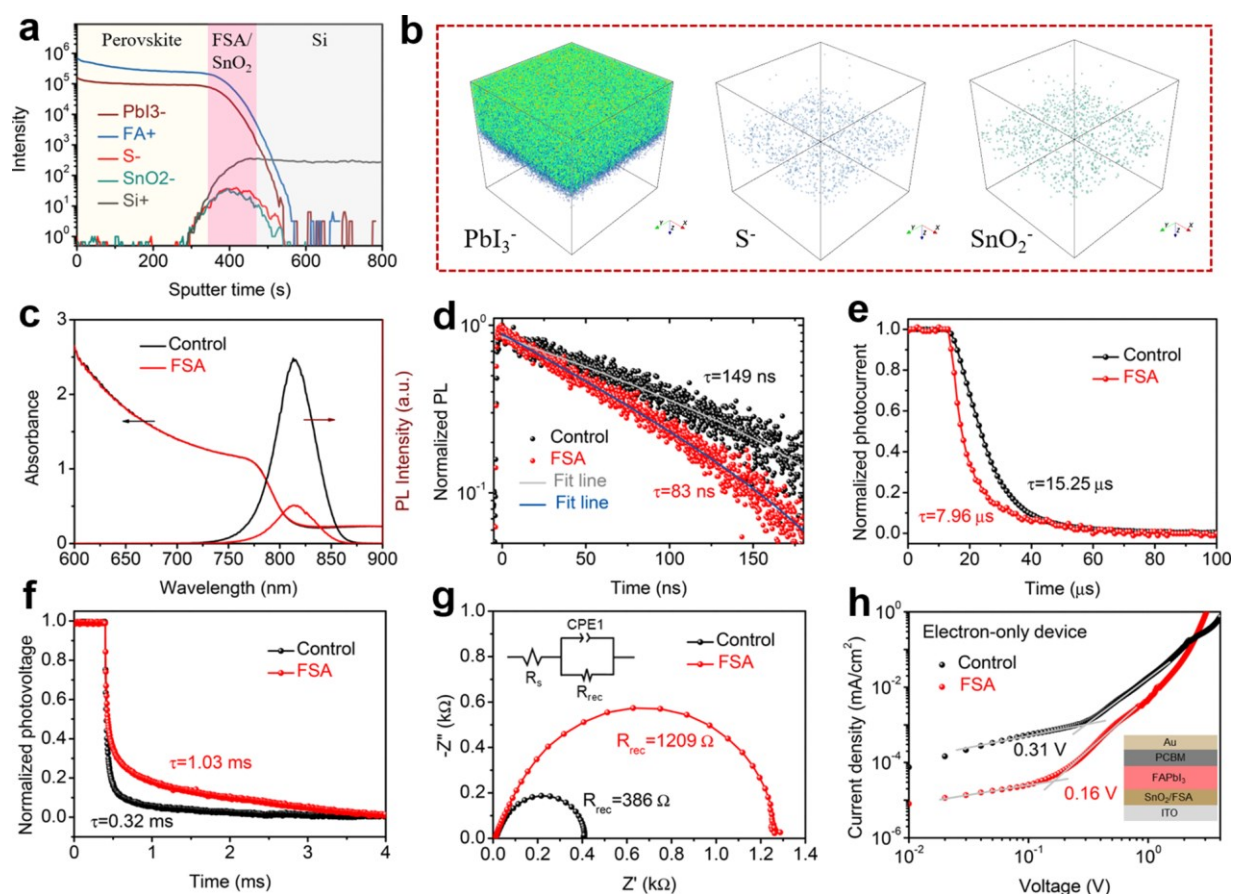
**Figure 3.** (a) ToF-SIMS depth profile and (b) the corresponding ion distribution of $PbI_3^-$, $S^-$, and $SnO_2^-$ in FSA-FAPbI$_3$ perovskite film. (c) UV-vis absorption and steady-state PL spectra, and (d) TRPL spectra of control and FSA-FAPbI$_3$ perovskite films. (e) TPC and (f) TPV curves of control and FSA-FAPbI$_3$ based devices. (g) Nyquist plots of control and FSA-FAPbI$_3$ based devices under dark condition at 0.8 V. Inset: the fitting circuit model. (h) Dark *J-V* measurement of control and FSA-FAPbI$_3$ based electron-only devices. Inset: schematic illustration of the device structure.

DFT calculations were further conducted to understand the underlying defect passivation mechanism realized by the addition of FSA. Previous reports have demonstrated that Pb-I antisite is one kind of deep-level charge trap that can lead to non-radiative recombination in PSCs.[26, 28] In general, Pb-I antisite defect forms more readily and predominate the surface of perovskite film because of its lower formation energy on surface.[29] The Pb-I antisite defect formation energy ($\Delta E_{defect}$) before and after FSA molecule adsorption on PbI$_2$-terminated (001) surface of FAPbI$_3$ perovskite were

then calculated in **Figure 4a**, where $E_{defect-system}$ and $E_{perfect-system}$ represent the total energies of FAPbI$_3$ perovskite system with and without Pb-I antisite defect, respectively. The higher $E_{defect-system}$ value of FSA-FAPbI$_3$ is ascribed to the strong interactions between the perovskite structure and FSA molecule, which leads to the increased Pb-I antisite defect formation energy. The $\Delta E_{defect}$ of FSA-FAPbI$_3$ perovskite system (2.572 eV) is higher than that of control system (0.502 eV), indicating that FSA-SnO$_2$ substrate can thermodynamically inhibit the formation of Pb-I antisite defect in FAPbI$_3$ perovskite. Besides, FSA-SnO$_2$ substrate can also passivate the formed Pb-I antisite defect at the SnO$_2$/perovskite interface. Herein, we simulated a Pb-I antisite defect on a PbI$_2$-terminated (001) surface that have a 2×2 periodicity in the *xy* plane, and the representative structure model can be found in **Figure 4b** and **Figure S17**. When FSA exists on the surface of perovskite, compared with a perfect perovskite surface, strong interactions between the perovskite with Pb-I antisite defect and FSA molecule are observed (**Figure 4c**), which leads to the charge redistribution at Pb-I antisite.[30] Additionally, the negative charge around the antisite I anion defect is delocalized owing to the electrostatic attraction with the positive center (-C(NH$_2$)$_2^+$ group) of FSA, which can suppress the migration of antisite I anion.[26] In summary, the -C(NH$_2$)$_2^+$ group in FSA molecule can interact with the [PbI$_6$]$^{4-}$ framework of perovskite, which will reduce the formation energy of deep-level charge defect. Besides, for the deep-level charge defect that had inevitably formed in the perovskite, the functional group in FSA can also suppress the migration of these defects. Therefore, it is believed that FSA-SnO$_2$ substrate can passivate the deep-level charge defect and reduce the non-radiative recombination in FSA-FAPbI$_3$ PSCs, thereby contributing to the realization of efficient and stable FAPbI$_3$ PSCs.
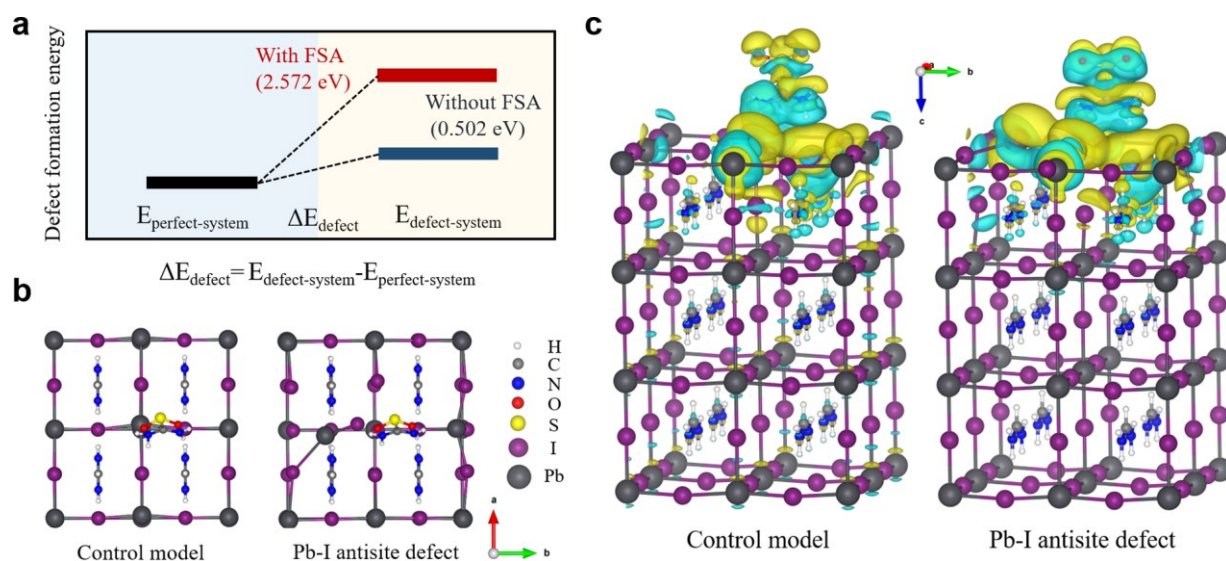
**Figure 4.** (a) Defect formation energy of Pb-I antisite before and after FSA adsorption on FAPbI$_3$ (001) surface. (b) Top view of theoretical models of FSA on FAPbI$_3$ (001) surface without and with Pb-I antisite defect. (c) Charge density difference of FSA on FAPbI$_3$ (001) surface without and with Pb-I antisite defect at isovalue of $5\times10^{-3}$ electrons/Å$^3$. Yellow indicates electron accumulation and blue indicates electron depletion.

We further explored the photovoltaic performance of the PSCs. Utilizing the proposed strategy, FAPbI$_3$ PSCs were fabricated using a configuration as illustrated in **Figure 5a**. The device performance with different concentrations of FSA treatment were investigated, and the results are summarized in **Figure S18** and **Table S3**. FAPbI$_3$ PSCs with or without FSA modification are denoted as control and target. **Figure 5b** shows *J-V* curves of the control and target PSCs under both forward and reverse scans. The control device had a maximum PCE of 22.1% with $J_{SC}$ of 25.06 mA/cm$^2$, $V_{OC}$ of 1.131 V and fill factor of 77.8%. The target PSC had a maximum PCE of 24.1% with $J_{SC}$ of 25.43 mA/cm$^2$, $V_{OC}$ of 1.166 V and fill factor of 81.3%. This PCE value is among the highest values for FAPbI$_3$ PSCs fabricated from sequential deposition (**Table S4**). The detail parameters are summarized in **Table 1**. The target PSC also exhibits a stabilized PCE output of 23.7% at the maximum power point of 0.99 V (**Figure S19**). Statistical distributions of the measured PCE of the control and target PSCs are displayed in **Figure 5c**. EQE$_{PV}$ measurements were performed to verify the measured $J_{SC}$ (**Figure 5d**). The EQE$_{PV}$ of the target

device was higher than that of the control device over the whole visible-light absorption region. By integrating the $EQE_{PV}$ over the AM 1.5G standard spectrum, the projected $J_{SC}$ of the control and target PSCs are 24.65 mA/cm$^2$ and 25.25 mA/cm$^2$, respectively, which well match the measured $J_{SC}$ under the solar simulator. To demonstrate the applicability and scalability of the FSA-FAPbI$_3$ PSC prepared through our modified sequential deposition approach, we also fabricated a cell with an enlarged area of 1 cm$^2$, which yields a high PCE of 21.4% with corresponding $J_{SC}$ of 25.15 mA/cm$^2$, $V_{OC}$ of 1.152 V and fill factor of 73.7% (**Figure 5e**).

It is known that the photovoltage of a solar cell is directly related to the ability to extract its internal electroluminescence (EL).[31] **Figure S20** shows the EL spectra of FSA-FAPbI$_3$ PSC, which were measured under different bias voltages in ambient conditions. An EL peak can be observed at 814 nm, which is consistent with the previous PL results. Typically, the voltage loss of PSC can be divided into radiative recombination voltage loss ($\Delta V_{rad}$) and non-radiative recombination voltage loss ($\Delta V_{non-rad}$). $\Delta V_{non-rad}$ is a key factor in dictating the final $V_{OC}$ of the device, which can be calculated by the following equation:[32]

$$\Delta V_{non-rad} = \frac{k\mathrm{T}}{q} \ln \frac{1}{EQE_{EL}}$$

Where $k$ is the Boltzmann constant, T is the temperature, $q$ is the electronic charge, and $EQE_{EL}$ is the external luminescence quantum efficiency. **Figure 5f** shows an $EQE_{EL}$ of 4.04% for an injection current density of 25.39 mA/cm$^2$ (corresponding to the $J_{SC}$ measured under 1 sun illumination). Thus, this result can be translated into a non-radiative loss as low as 81 mV. For comparison, the control device shows an $EQE_{EL}$ of 1.39% for an injection current density of 25.21 mA/cm$^2$ (**Figure S21**), which suggests a much higher non-radiative loss in the control device. Since stability issues remain the main obstacle to the commercialization of PSCs, we further investigated the operational stability of the PSCs by aging the unencapsulated devices using maximum power point (MPP) tracking, which was conducted under a simulated 1 sun illumination in nitrogen atmosphere. **Figure 5g** shows the PCE of the PSCs under

continuous light soaking for 1000 h. The control device underwent a 60% PCE loss within only 600 h, whereas the target cell only lost around 15% of its initial efficiency over 1000 h. Note that we did not cool the cells during illumination, the temperature of the PSCs was measured to be around 50°C during this experiment. Based on the photographs in **Figure 5g**, we suspect that the degradation of FAPbI$_3$ at the SnO$_2$ ETL/perovskite interface is the main reason for the decreased efficiency under continuous illumination. To further investigate the thermal stability of the control and FSA-FAPbI$_3$ films, we kept the films aging at 100 °C in N$_2$ glove box for 500 h. As displayed in **Figure S22**, similar UV-vis absorption profiles are observed for both films after the first 100 h. However, the FSA-FAPbI$_3$ sample exhibits much better thermal stability after 500 h of thermal treatment. This result demonstrates that the degradation of FAPbI$_3$ at higher temperature can also be suppressed by FSA-SnO$_2$ substrate.
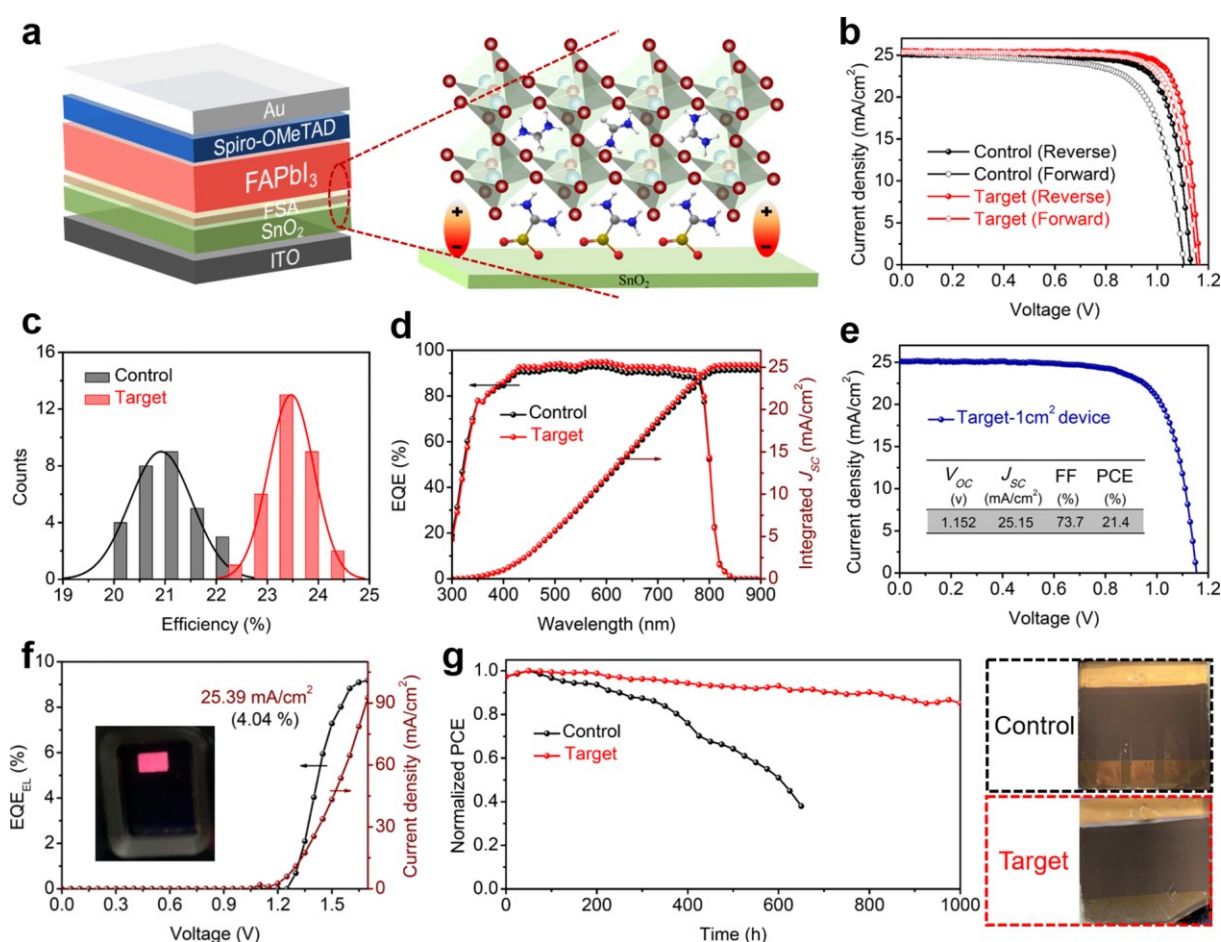
**Figure 5.** (a) Schematic structure of the FSA-FAPbI$_3$ based device and FSA induced dipole moment at the SnO$_2$/perovskite interface. (b) *J-V* curves of target and control FAPbI$_3$ PSCs under both reverse and forward scan directions. (c) Statistical distribution of the PCEs of the target and control FAPbI$_3$ PSCs. (d) EQE spectra and the corresponding integrated *J$_{SC}$* of the target and control FAPbI$_3$ PSCs. (e) *J-V* curves of target FAPbI$_3$ PSCs with a 1 cm$^2$ active area. (f) EQE$_{EL}$ and current density of FSA-FAPbI$_3$ PSCs under bias voltage from 0 to 1.7V. Inset:  photograph of the luminescence of FSA-FAPbI$_3$ PSCs under bias voltage. (g) MPP-tracking measured with the target and control FAPbI$_3$ PSCs under full solar illumination (AM 1.5G, 100 mW/cm$^2$ in N$_2$ condition at 50-60°C. Inset: photographs of the target and control FAPbI$_3$ devices taken from the FTO side after the MPP-tracking.

**Table 1.** Photovoltaic parameters of champion PSCs with or without FSA modification.

| Sample | Scan direction | *V$_{OC}$* (V) | *J$_{SC}$* (mA/cm$^2$) | FF (%) | PCE (%) |
|---|---|---|---|---|---|
| Control | Reverse | 1.131 | 25.06 | 77.8 | 22.1 |
|  | Forward | 1.105 | 25.29 | 70.1 | 19.6 |
| Target | Reverse | 1.166 | 25.43 | 81.3 | 24.1 |
|  | Forward | 1.157 | 25.36 | 78.8 | 23.2 |

## 3. Conclusion

Overall, we have developed a strategy of zwitterion-functionalized substrate induced sequential deposition to obtain the highly efficient and stable FAPbI$_3$ PSCs using FSA-SnO$_2$ ETL. From the characterization of FSA-SnO$_2$ ETL and related theoretical calculation, we have demonstrated that FSA zwitterion can act as interfacial dipole to optimize the energy level alignment and enhance the conductivity of SnO$_2$ ETL, suppressing the charge recombination and accelerating electron extraction at the perovskite/SnO$_2$ interface. Additionally, FSA-SnO$_2$ substrate can rearrange the stack direction and orientation of residual PbI$_2$, as well as inhibiting the residual PbI$_2$ at the perovskite/SnO$_2$ interface,

thus reducing the side effect of the residual PbI$_2$. Furthermore, the characterizations and DFT calculations on FAPbI$_3$ elucidate that FSA-SnO$_2$ substrate can inhibit the formation of deep-level charge defects and reduce the non-radiative recombination in FAPbI$_3$ PSCs. These characteristics enables the fabrication of highly efficient and stable black phase FAPbI$_3$ PSC with an excellent PCE up to 24.1% and a non-radiative loss as low as 81 mV, as well as 1000 h of long-term operational stability. This study provides a new interface engineering strategy to the sequential fabrication of black phase FAPbI$_3$ PSCs with improved stability and optoelectronic performance.

**4. Experimental Section**

*Materials.*

All commercial materials were used as-received without any further purification. Tin (IV) oxide colloid solution (SnO$_2$, 15wt%) and lead iodide (PbI$_2$, 99.999%) were purchased from Alfa Aesar. Formamidinium iodide (FAI, 99.5%) was purchased from Xi'an Polymer Light Technology Corp., China. Dimethylformamide (DMF, 99.8%), dimethylsulfoxide (DMSO, 99.9%), isopropanol (IPA, 99.8%), chlorobenzene (CB, 99.8%), 4-tert-butylpyridine (tBP, 96%), bis (trifluoromethane) sulfonamide lithium salt (Li-TFSI, 99.95%), and spiro-OMeTAD (99.7%) were purchased from Sigma Aldrich. Formamidine sulfinic acid (FSA, 99.5%) was purchased from TCI.

*Device Fabrication.*

ITO substrates were sonicated in DI water, IPA and ethanol sequentially. Then, ITO substrates were blown dry with nitrogen and treated with UV-ozone for 10 min. After that, SnO$_2$ colloid solution was spin-coated on the substrates at 3000 rpm for 30 s, and then heated at 180°C for 30 min. For FSA-SnO$_2$ films, FSA solution with different concentrations (1, 3, 6 mg/mL) was spin-coated on the SnO$_2$ film at 3000 rpm for 30 s, followed by annealing at 100°C for 5 min. PbI$_2$ solution was spun cast onto the SnO$_2$ at 1500 rpm for 30 s, followed by annealing at 100°C for 60 s. Then, the organic ammonium salt solution was spin-coated on the PbI$_2$ film at 2000 rpm for 30 s and heated in ambient air at 150°C for 15 min.

# WILEY-VCH

Upon cooling to room temperature, the PEAI (5 mg/mL in IPA) was spin coated on the perovskite at 5000 rpm for 30s without annealing. Subsequently, spiro-OMeTAD solution was deposited on top of the perovskite layer by spin coating at 3000 rpm for 25 s. Finally, 80 nm Au was thermal evaporated as electrode on top of film.

*Films Characterization.*

The chemical states of $SnO_2$ and $FSA-SnO_2$ films were characterized by XPS (Kratos AXIS ULTRA HAS, monochromated Al K$\alpha$ = 1486.6 eV). Analysis of the XPS data was performed using Casa XPS 2.3.16 software. The electronic properties of $SnO_2$ and $FSA-SnO_2$ films were complemented by UPS (Kratos AXIS ULTRA HAS, He-I$\alpha$ = 21.22 eV). The time acquisition for each scan in UPS was 15 s. The binding energy values for XPS and UPS were calibrated by measuring Au $4f_{7/2}$ (84.0 eV) and Fermi edge ($E_F$=0 eV) on a clean Au surface, respectively. The crystal structures of as-prepared perovskite films were characterized using Shimadzu XRD-6100 diffractometer with Cu K$\alpha$ radiation. The AFM, c-AFM and KPFM images for ETL surfaces were obtained using an atomic force microscope (Dimension Icon, BRUKER, USA). A multi-75E-G probe (PF TUNA) was used for c-AFM detection. KPFM images were obtained using a conductive Antimony (n) doped Si Rtespa-300 probe with the frequency of 300 kHz and spring constants of 30 N/m. The UV-vis spectra of ETLs and perovskite films were measured on an Agilent Cary 60 UV-vis spectrophotometer. GIWAXS measurements were performed at the BL14B1 beamline of the Shanghai Synchrotron Radiation Facility (SSRF) using X-rays with a wavelength of 1.2398 Å. 2D GIWAXS patterns were acquired by a MarCCD detector mounted vertically at a distance of 260 nm form the sample with a grazing incidence angle of 0.3° and an exposure time of 50 s. The 2D GIWAXS patterns were analyzed using the FIT2D software and displayed in scattering vector $q$ ($q$=4$\pi$sin$\theta$/$\lambda$) coordinates. The SEM and cross-sectional SEM images were acquired by scanning electron microscopy (JEOL JSM-7800F Prime). The elemental distribution in perovskite film was characterized using TOF-SIMS 5100 ION-TOF GmbH, Germany. Steady-state PL and TRPL spectra were recorded using a spectrophotometer (FLS1000) operated at 435 nm excitation.

**References**

[1] N.-G. Park, M. Grätzel, T. Miyasaka, K. Zhu, K. Emery, *Nat. Energy* 2016, *1*, 16152.

[2] Y. Wang, M. I. Dar, L. K. Ono, T. Zhang, M. Kan, Y. Li, L. Zhang, X. Wang, Y. Yang, X. Gao, Y. Qi, M. Grätzel, Y. Zhao, *Science* 2019, *365*, 591.

[3] J.-P. Correa-Baena, M. Saliba, T. Buonassisi, M. Grätzel, A. Abate, W. Tress, A. Hagfeldt, *Science* 2017, *358*, 739.

[4] G. E. Eperon, S. D. Stranks, C. Menelaou, M. B. Johnston, L. M. Herz, H. J. Snaith, *Energy Environ. Sci.* 2014, *7*, 982.

[5] N. J. Jeon, J. H. Noh, W. S. Yang, Y. C. Kim, S. Ryu, J. Seo, S. I. Seok, *Nature* 2015, *517*, 476.

[6] H. Lu, Y. Liu, P. Ahlawat, A. Mishra, R. Tress Wolfgang, T. Eickemeyer Felix, Y. Yang, F. Fu, Z. Wang, E. Avalos Claudia, I. Carlsen Brian, A. Agarwalla, X. Zhang, X. Li, Y. Zhan, M. Zakeeruddin Shaik, L. Emsley, U. Rothlisberger, L. Zheng, A. Hagfeldt, M. Grätzel, *Science* 2020, *370*, eabb8985.

[7] G. Kim, H. Min, S. Lee Kyoung, Y. Lee Do, M. Yoon So, I. Seok Sang, *Science* 2020, *370*, 108.

[8] F. Ye, J. Ma, C. Chen, H. Wang, Y. Xu, S. Zhang, T. Wang, C. Tao, G. Fang, *Adv. Mater.* 2021, *33*, 2007126.

[9] Q. Jiang, L. Zhang, H. Wang, X. Yang, J. Meng, H. Liu, Z. Yin, J. Wu, X. Zhang, J. You, *Nat. Energy* 2016, *2*, 16177.

[10] X. Yang, Y. Fu, R. Su, Y. Zheng, Y. Zhang, W. Yang, M. Yu, P. Chen, Y. Wang, J. Wu, D. Luo, Y. Tu, L. Zhao, Q. Gong, R. Zhu, *Adv. Mater.* 2020, *32*, 2002585.

[11] S. Wang, J. Jin, Y. Qi, P. Liu, Y. Xia, Y. Jiang, R.-X. He, B. Chen, Y. Liu, X.-Z. Zhao, *Adv. Funct. Mater.* 2020, *30*, 1908343.

[12] N. Pellet, P. Gao, G. Gregori, T.-Y. Yang, M. K. Nazeeruddin, J. Maier, M. Grätzel, *Angew. Chem. Int. Ed.* 2014, *53*, 3151.

[13] D. J. Slotcavage, H. I. Karunadasa, M. D. McGehee, *ACS Energy Lett.* 2016, *1*, 1199.

[14] S. Draguta, O. Sharia, S. J. Yoon, M. C. Brennan, Y. V. Morozov, J. S. Manser, P. V. Kamat, W. F. Schneider, M. Kuno, *Nat. Commun.* 2017, *8*, 200.

[15] Q. Jiang, Z. Chu, P. Wang, X. Yang, H. Liu, Y. Wang, Z. Yin, J. Wu, X. Zhang, J. You, *Adv. Mater.* 2017, *29*, 1703852.

[16]    T. J. Jacobsson, J.-P. Correa-Baena, E. Halvani Anaraki, B. Philippe, S. D. Stranks, M. E. F. Bouduban, W. Tress, K. Schenk, J. Teuscher, J.-E. Moser, H. Rensmo, A. Hagfeldt, *J. Am. Chem. Soc.* 2016, *138*, 10331.

[17]    G. Tumen-Ulzii, C. Qin, D. Klotz, M. R. Leyden, P. Wang, M. Auffray, T. Fujihara, T. Matsushima, J.-W. Lee, S.-J. Lee, Y. Yang, C. Adachi, *Adv. Mater.* 2020, *32*, 1905035.

[18]    L. Zuo, Z. Gu, T. Ye, W. Fu, G. Wu, H. Li, H. Chen, *J. Am. Chem. Soc.* 2015, *137*, 2674.

[19]    B. Tu, Y. Shao, W. Chen, Y. Wu, X. Li, Y. He, J. Li, F. Liu, Z. Zhang, Y. Lin, X. Lan, L. Xu, X. Shi, A. M. C. Ng, H. Li, L. W. Chung, A. B. Djurišić, Z. He, *Adv. Mater.* 2019, *31*, 1805944.

[20]    K. Choi, J. Lee, H. I. Kim, C. W. Park, G.-W. Kim, H. Choi, S. Park, S. A. Park, T. Park, *Energy Environ. Sci.* 2018, *11*, 3238.

[21]    Z. Xu, Z. Liu, N. Li, G. Tang, G. Zheng, C. Zhu, Y. Chen, L. Wang, Y. Huang, L. Li, N. Zhou, J. Hong, Q. Chen, H. Zhou, *Adv. Mater.* 2019, *31*, 1900390.

[22]    W. Hui, L. Chao, H. Lu, F. Xia, Q. Wei, Z. Su, T. Niu, L. Tao, B. Du, D. Li, Y. Wang, H. Dong, S. Zuo, B. Li, W. Shi, X. Ran, P. Li, H. Zhang, Z. Wu, C. Ran, L. Song, G. Xing, X. Gao, J. Zhang, Y. Xia, Y. Chen, W. Huang, *Science* 2021, *371*, 1359.

[23]    B.-w. Park, N. Kedem, M. Kulbak, D. Y. Lee, W. S. Yang, N. J. Jeon, J. Seo, G. Kim, K. J. Kim, T. J. Shin, G. Hodes, D. Cahen, S. I. Seok, *Nat. Commun.* 2018, *9*, 3301.

[24]    B. Shi, X. Yao, F. Hou, S. Guo, Y. Li, C. Wei, Y. Ding, Y. Li, Y. Zhao, X. Zhang, *J. Phys. Chem. C* 2018, *122*, 21269.

[25]    Z. Qin, Y. Chen, X. Wang, X. Liu, Y. Miao, Y. Zhao, *J. Phys. Chem. Lett.* 2021, *12*, 6883.

Accepted Article

[26] X. Zheng, B. Chen, J. Dai, Y. Fang, Y. Bai, Y. Lin, H. Wei, Xiao C. Zeng, J. Huang, *Nat. Energy* 2017, *2*, 17102.

[27] R. H. Bube, *J. Appl. Phys.* 1962, *33*, 1733.

[28] W. S. Yang, B.-W. Park, E. H. Jung, N. J. Jeon, Y. C. Kim, D. U. Lee, S. S. Shin, J. Seo, E. K. Kim, J. H. Noh, S. I. Seok, *Science* 2017, *356*, 1376.

[29] A. Abate, M. Saliba, D. J. Hollman, S. D. Stranks, K. Wojciechowski, R. Avolio, G. Grancini, A. Petrozza, H. J. Snaith, *Nano Lett.* 2014, *14*, 3247.

[30] W. Fan, S. Zhang, C. Xu, H. Si, Z. Xiong, Y. Zhao, K. Ma, Z. Zhang, Q. Liao, Z. Kang, Y. Zhang, *Adv. Funct. Mater.* 2021, *31*, 2104633.

[31] R. T. Ross, *J. Chem. Phys.* 1967, *46*, 4590.

[32] Q. Jiang, Y. Zhao, X. Zhang, X. Yang, Y. Chen, Z. Chu, Q. Ye, X. Li, Z. Yin, J. You, *Nat. Photonics* 2019, *13*, 460.

**A zwitterion formamidine sulfinic acid (FSA)** is deposited at the $SnO_2$/perovskite interface to induce the crystallization of high-quality black phase $FAPbI_3$ via sequential deposition. The FSA-$SnO_2$ substrate can also help **reduce the side effect of the residual $PbI_2$** and suppress the interfacial deep-level defects, yielding an impressive PCE of 24.1% and 1000 h long-term operational stability.

Zhixiao Qin[a], Yuetian Chen[a], Xingtao Wang[a], Ning Wei[a], Xiaomin Liu[a], Haoran Chen[a], Yanfeng Miao[a], and Yixin Zhao[a,b]*

**Zwitterion-functionalized $SnO_2$ Substrate Induced Sequential Deposition of Black Phase $FAPbI_3$ with Rearranged $PbI_2$ Residue**

ToC figure ((Please choose one size: 55 mm broad × 50 mm high **or** 110 mm broad × 20 mm high. Please do not use any other dimensions))